JOURNAL OF PROPULSION AND POWER
Vol. 22, No. 3, May–June 2006

Hypersonic Aerodynamic Control and Thrust Vectoring by Nonequilibrium Cold-Air Magnetohydrodynamic Devices

Mikhail N. Shneider* and Sergey O. Macheret†
Princeton University, Princeton, New Jersey 08544

A theoretical investigation of hypersonic aerodynamic control with cold-air magnetohydrodynamic (MHD) devices was conducted for an inviscid flat-plate flow. The magnetic field is either perpendicular or directed at an angle to the plate. The cold hypersonic flow is ionized by electron beams injected along the magnetic field lines. The accelerating or decelerating Lorentz forces together with the joule heating of the flow can ensure both angle-of-attack and steering control. The profiles of tangential forces are shown to vary dramatically with the ratio χ of the applied electric field to the product of freestream velocity and the magnetic field at the surface, from predominantly decelerating forces (drag) at low χ to a combination of deceleration near the surface and acceleration of the outer flow at $\chi \approx 0.5$, to only acceleration (thrust) at $\chi = 1$. Varying the tilt angle of the magnetic field is shown to increase the flexibility of MHD control. The normal (lift) force created by the MHD region is shown to be substantially stronger than the drag/thrust force, with the lift/drag (for MHD generators) or lift/thrust (for accelerators) ratios increasing from about two with magnetic field tilted against the flow or normal to the surface to more than three with aft-tilted magnetic field.

Nomenclature

$\boldsymbol{B}$	=	magnetic field vector
B_z	=	z component of the magnetic field
B_0	=	maximum value of the magnetic field
E_x, E_y	=	x and y components of the electric field
e	=	electron charge
$F_{f,i}$	=	friction force per ion
$F_{L,e}$, $L_{L,i}$	=	Lorentz forces acting on an electron and an ion, respectively
F_x, F_z	=	tangential and normal forces on the surface, respectively
$\boldsymbol{j}$	=	electric current density
j_b	=	current density of the electron beam at the injection point
j_y	=	current density component along y axis
k	=	load factor
L_b	=	electron beam penetration length
M	=	Mach number
M_{in}	=	ion-neutral reduced mass
m	=	mass of electron
N_x, N_z	=	number of grid points in x and z directions, respectively
n_b	=	number density of beam electrons
n_e	=	number density of plasma electrons
P_b	=	heating rate due to electron beams
P_J	=	joule heating rate
$P_{j\times B}$	=	rate of work done by Lorentz forces
P_{MHD}	=	magnetohydrodynamic (MHD) power deposition or extraction rate
P_{vib}	=	power spent on vibrational excitation of molecules
Q_b	=	electron beam power deposition density
q	=	dynamic pressure
p	=	static pressure
p_0	=	freestream static pressure
R_M	=	effective radius of the magnetic coil
T	=	translational–rotational static gas temperature
T_v	=	vibrational temperature
T_0	=	freestream static temperature
$\boldsymbol{u}$	=	gas velocity
$u_{e,y}$, $u_{i,y}$	=	electron and ion drift velocities along y axis
u_{px}	=	x component of the plasma (ion–electron) velocity
u_x	=	x component of the gas velocity
u_0	=	freestream velocity
$X_{\max}$	=	length of computational domain in x direction
x	=	coordinate
y	=	coordinate
$Z_{\max}$	=	size of computational domain in z direction
z	=	coordinate
α	=	tilt angle of the magnetic field lines with respect to the surface
γ	=	increment of beam-plasma instability
ΔD	=	change in drag force
ΔL	=	change in lift force
Δx_{MHD}	=	length of MHD region
ε_b	=	initial energy of beam electrons
μ_e, μ_i	=	electron and ion mobilities
ν_{en}	=	electron–molecule collision frequency
ν_{in}	=	ion–molecule collision frequency
ρ	=	gas density
σ	=	scalar electrical conductivity
$\tilde{\sigma}$	=	effective electrical conductivity corrected for ion slip
χ	=	ratio of the applied electric field to the product of freestream velocity and the magnetic field at the surface
Ω_e	=	electron Hall parameter
Ω_+	=	ion Hall parameter
$\tilde{\Omega}$	=	effective Hall parameter corrected for ion slip
ω_p	=	plasma oscillation frequency

Presented as Paper 2005-0979 at the AIAA 43rd Aerospace Sciences Meeting and Exhibit, Reno, NV, 10–13 January, 2005; received 4 April 2005; revision received 10 September 2005; accepted for publication 11 September 2005.

*Research Scientist, Department of Mechanical and Aerospace Engineering, D-414 Engineering Quadrangle. Senior Member AIAA.

†Senior Research Scientist, Department of Mechanical and Aerospace Engineering, D-418 Engineering Quadrangle; macheret@princeton.edu. Associate Fellow AIAA.

I. Introduction

IN the last several years, a number of studies have explored potential performance of hypersonic magnetohydrodynamic (MHD) devices for onboard power generation, inlet control, and energy

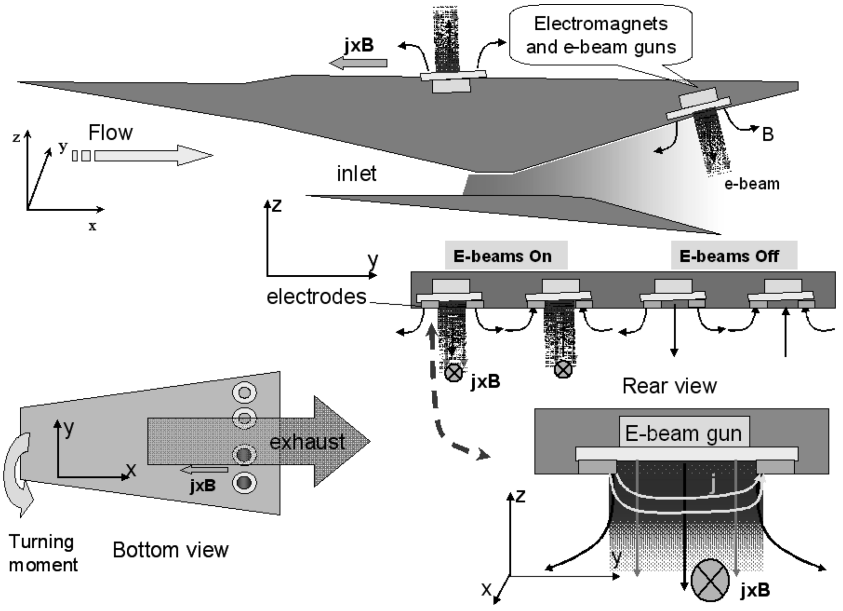

Fig. 1 Schematic of proposed MHD aerodynamic control and thrust vectoring concept.

bypass for scramjets.[1–13] As shown in previous papers,[1–6] unless the MHD device is collocated with the combustor or positioned immediately downstream of it, the necessary ionization in the MHD region at flight Mach numbers below 12 must be generated artificially. The energy cost of ionization determines the design and performance envelope of the device.[1–6] The minimization of the ionization power budget necessitates the use of electron beams (or, in some cases, repetitive high-voltage nanosecond pulses) for ionization.[1–6] Despite the high ionization efficiency, however, the use of MHD devices with electron beams for the global control of propulsion systems and for power extraction along the propulsion flowpath is problematic. This is due to a combination of factors, including the loss of stagnation pressure and thrust resulting from joule dissipation and energy extraction, and the weight and complexity associated with the large-scale MHD devices and magnets.

In the present paper, we explore another potential application of cold-air MHD processes: aerodynamic control and thrust vectoring. The concept is shown schematically in Fig. 1. Arrays of MHD devices with electron beam ionization are positioned at the bottom of the vehicle aft of the combustor, where the density is close to that in the freestream, and/or on the top of the vehicle. The cold hypersonic flow is ionized by electron beams injected along the magnetic field lines, and an MHD generator or accelerator is operated with electrodes either placed on sidewalls (not shown in Fig. 1) or mounted flush with the vehicle surface (as in Fig. 1). The $\boldsymbol{j} \times \boldsymbol{B}$ forces together with the joule heating of the flow can ensure both angle-of-attack and steering control (the latter by selectively turning on only some parts of the MHD array), as shown in Fig. 1, thus acting as MHD virtual flaps. Note that Fig. 1 only shows decelerating $\boldsymbol{j} \times \boldsymbol{B}$ forces, corresponding to the MHD generator case. In principle, when an appropriate electric field is applied and electric power is spent, the $\boldsymbol{j} \times \boldsymbol{B}$ forces would accelerate the flow. The MHD accelerator regime is also studied in this paper.

The high flow velocities and low densities would assure the efficient functioning of the MHD devices.[1–6] Indeed, at a constant load factor, the magnitude of $\boldsymbol{j} \times \boldsymbol{B}$ force is proportional to the flow velocity and to the electrical conductivity. Because the electrical conductivity is proportional to the ratio of electron number density and the gas number density, and the ionization power budget is proportional to the square of electron density, it is advantageous to place the MHD devices in the regions of high velocity and low density.

II. Model

A. MHD Model

In this work, preliminary studies of forces that could be generated in the devices shown in Fig. 1 were conducted for a flat-plate two-dimensional inviscid flow of an ideal gas and an ideal Faraday, that is, with zero Hall current, MHD generator or accelerator. The MHD equations, electron beam ionization model, three-species (electrons, positive ions, and negative ions) plasma kinetics, and kinetics of vibrational excitation and relaxation were those of Refs. 2, 3, and 5, as modified in Ref. 6, and were coupled with two-dimensional compressible inviscid flow equations.

In the low-density, strong magnetic field environment typical for the cases considered in this work, electron Hall parameter can be quite high and the ion slip can be significant. Additionally, nonuniform flow velocity and magnetic field require generalization of MHD equations. For the generator regime, the ion slip corrections, consisting in the use of effective Hall and ion slip parameters,[14] are described in Refs. 2, 3, 5, and 6 and the generalization for nonuniform velocity and magnetic field in Ref. 6. To derive the corrections to MHD equations due to the ion slip, consider the physics of MHD acceleration of weakly ionized plasma in an ideal Faraday accelerator.

Let the magnetic field B_z be directed along the z axis and the electric field E_y along the y axis. The velocity of the bulk neutral gas, u_x, and the plasma (ion–electron) velocity u_{px} are directed along x. The electric field in the reference frame moving at the velocity equal to u_{px} is $(E_y - u_{px}B_z)$, and electrons and ions acquire drift velocities normal to the flow with the absolute values

$$u_{e,y} = \mu_e(E_y - u_{px}B_z), \qquad u_{i,y} = \mu_i(E_y - u_{px}B_z) \tag{1}$$

where μ_e and μ_i are the electron and ion mobilities. These drift velocities have, of course, opposite directions. The electron and ion drift velocities give rise to the x-directed accelerating Lorentz forces on an electron and an ion,

$$F_{L,e} = eu_{e,y}B_z = e\mu_e B_z(E_y - u_{px}B_z) = e\Omega_e(E_y - u_{px}B_z) \tag{2}$$

$$F_{L,i} = eu_{i,y}B_z = e\mu_i B_z(E_y - u_{px}B_z) = e\Omega_i(E_y - u_{px}B_z) \tag{3}$$

where $\Omega_e = \mu_e B_z$ and $\Omega_i = \mu_i B_z$ are the electron and ion Hall parameters. Because the electron mobility greatly exceeds the ion mobility, the electrons experience a much greater accelerating force. Their separation from ions is prevented by the plasma polarization

that creates an electric field "gluing" the electrons and ions and maintaining the quasi neutrality. When electron inertia is neglected, the accelerating force $F_{L,e}$ must be balanced by the retarding force due to the polarization field and the force of "friction" of an electron against the bulk neutral gas. The latter can be shown a posteriori to be negligible compared to the force exerted by the polarization field because $\Omega_e \gg \Omega_i$. Thus, the polarization field is

$$E_x = \Omega_e(E_y - u_{px}B_z) \tag{4}$$

which is, of course, the familiar Hall field. The ions are pulled forward by both the Lorentz force (3) and by the force exerted by the Hall field. Because $\Omega_e \gg \Omega_i$, the former is negligible in comparison with the latter. Thus, the force exerted by the Hall field on the ions is transferred to the neutrals as a result of a ion–neutral friction. The friction force per ion is

$$F_{f,i} = M_{in}\nu_{in}(u_{px} - u_x) = (e/\mu_i)(u_{px} - u_x)$$
$$= (eB/\Omega_i)(u_{px} - u_x) \tag{5}$$

where ν_{in} is the ion-neutral collision frequency. Equating the friction force from Eq. (5) and the pulling force eE_x with E_x from Eq. (4), we obtain the formula for ion–electron convective velocity,

$$u_{px} = \frac{u_x + \Omega_e\Omega_i(E_y/B_z)}{1 + \Omega_e\Omega_i} \tag{6}$$

As seen from Eq. (6), when the ion slip parameter $\Omega_e\Omega_i$ is small, the ion–electron (plasma) convective velocity is indeed close to that of the bulk neutral gas. In the limit $\Omega_e\Omega_i \gg 1$, the plasma velocity reaches the value determined by the drift of single charged particles (without collisions) in the crossed electric and magnetic fields: $u_{px} \approx E_y/B_z$. When the bulk gas velocity approaches the limit E_y/B_z, then both u_x and u_{px} are close to that limit and to each other.

When Eq. (6) is used, the Hall electric field and the Faraday current density can be expressed as

$$E_x = \Omega_e(E_y - u_{px}B_z) = [\Omega_e/(1 + \Omega_e\Omega_i)](E_y - u_xB_z)$$
$$= \tilde{\Omega}(E_y - u_xB_z) \tag{7}$$

$$j_y = \sigma(E_y - u_{px}B_z) = [\sigma/(1 + \Omega_e\Omega_i)](E_y - u_xB_z)$$
$$= \tilde{\sigma}(E_y - u_xB_z) \tag{8}$$

so that the conventional MHD equations operating with the velocity u_x are valid; if, instead of the Hall parameter Ω_e and the conductivity σ, their effective values are used

$$\tilde{\Omega} = \Omega_e/(1 + \Omega_e\Omega_i), \qquad \tilde{\sigma} = \sigma/(1 + \Omega_e\Omega_i) \tag{9}$$

These formulas for effective Hall parameter and conductivity values turn out to be the same as in the generator case.[14] However, Eq. (6) for the ion–electron (plasma) convective velocity that should be used in the kinetic equation for electron balance is different from that in the generator case.[2,3,5,6]

In the case of nonuniform velocity and magnetic field, Ohm's law (8) applies with local values of conductivity, velocity, magnetic field, and Hall parameters. However, the electric field strength E_y is a global quantity in a sense that it is constant throughout the MHD region, as dictated by the equation $\nabla \times \boldsymbol{E} = 0$. Therefore, depending on the value of E_y, some regions of the flow would have a positive current and would experience acceleration, whereas in other regions, where $u_xB_z < E_y$, the current would be reversed, resulting in decelerating j_yB_z force. Only when $E_y \geq u_0B_0$, where u_0 and B_0 are the maximum values of u_x and B_z, the entire MHD region would experience accelerating j_yB_z forces. Note that the conventional definition of the load factor as the ratio $k = E_y/uB$ cannot be applied in the nonuniform flowfield case because different points would have their own load factors. Instead, because in the case of an accelerator the imposed electric field E_y is a primary variable, in this work we use a well-defined parameter $\chi = E_y/u_0B_0$, which should not be called the load factor. In the generator cases, the load factor can be defined through the ratio of load resistance and the integrated resistance of the nonuniform plasma region, as discussed in Ref. 6. Thus, in the generator cases to be described, the load factor serves as a primary variable, and the electric field E_y is computed with the formulas of Ref. 6.

B. Configuration, Conditions, and Parameter Ranges

The geometry for all cases computed in this work is shown in Fig. 2. The magnetic field was assumed to be tilted at an angle α with respect to the horizontal surface, and because the electron beams would follow the lines of magnetic field, the entire plasma region is also tilted at the angle α. The strength of magnetic field was a decreasing function of the distance along its direction from the surface; the function was that of the magnetic field along the axis of a coil with the radius $R_M = 0.5$ m[6], and the maximum magnetic field strength (at the surface) was $B_0 = \sqrt{[B_x(z=0)^2 + B_z(z=0)^2]} = 3$ T. The magnetic field was assumed uniform in both the x and y directions. The plasma region had the length $\Delta x_{\mathrm{MHD}} = 0.15$ m along the flow. Strictly speaking, the magnetic field used in this paper is not divergence free. The physical approximation used here is the neglect of tangential components (in our two-dimensional case, x components) of the field and their variation with x. Because the MHD region (0.15 m long along the flow) is concentrated very close to the centerline of the 1-m-diam coil, the magnetic field in this region should be close to that on the centerline. Thus, although the zero-divergence condition is not strictly satisfied, the error due to the neglect of tangential components of the field is expected to be small.

The electron beams were assumed to have such an energy spectrum that the beam-induced ionization rate is uniform in the entire plasma region,[6] from the vehicle surface to the distance $L_b = 0.65$ m from the surface. The lateral scattering of the beam electrons was assumed to be suppressed by the strong magnetic field. Depending on the flow parameters, the maximum electron beam energy was $\varepsilon_b \leq 25$ keV, and the beam current density varied from $j_b \approx 260$ to $j_b \approx 1300$ A/m^2. The ratio of number densities of beam and plasma electrons, n_b/n_e, in the cases considered in this paper (Sec. III) is on the order of 10^{-5}. At the electron density $n_e \approx 6 \times 10^{12}$ cm^{-3} (Sec. III), the plasma frequency $\omega_p \approx 1.4 \times 10^{11}$ s^{-1} exceeds the electron–molecule collision frequency (when in a typical case $\nu_{en} \approx 1.2 \times 10^{10}$ s^{-1}) by an order of magnitude. However, the maximum increment of beam-plasma instability $\gamma = \omega_p(n_b/n_e)^{1/3} \approx 3 \times 10^9$ s^{-1} is smaller than the collision frequency. Therefore, the beam-plasma instability is well damped, and the collisional ionization model of Refs. 2, 3, 5, and 6 is applicable.

The freestream flow conditions in the principal MHD cases corresponded to Mach 8 flight at dynamic pressure of $q =$ 1000 psf (47.88 kPa): the static pressure and temperature were $p_0 = 1068.75$ Pa and $T_0 = 227.26$ K, and the freestream velocity was $u_0 = 2417.9$ m/s. Additional cases were run at Mach 6, 7, and 10 with the same dynamic pressure of $q = 1000$ psf (47.88 kPa).

The maximum values of Hall and ion slip parameters in the computed cases were $\Omega_{e,\max} \approx 11$ and $(\Omega_e\Omega_i)_{\max} \approx 0.3$ at Mach 8 and $\Omega_{e,\max} \approx 17.3$ and $(\Omega_e\Omega_i)_{\max} \approx 0.66$ at Mach 10.

The governing equations were solved with the second-order marching McCormack scheme. The size of the computational domain, $X_{\max} \times Z_{\max}$, was dictated by the two requirements: that the

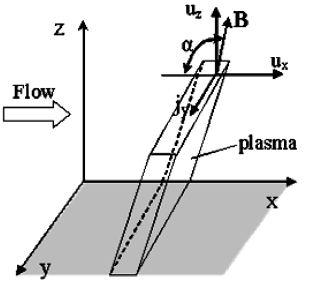

Fig. 2 Computational geometry.

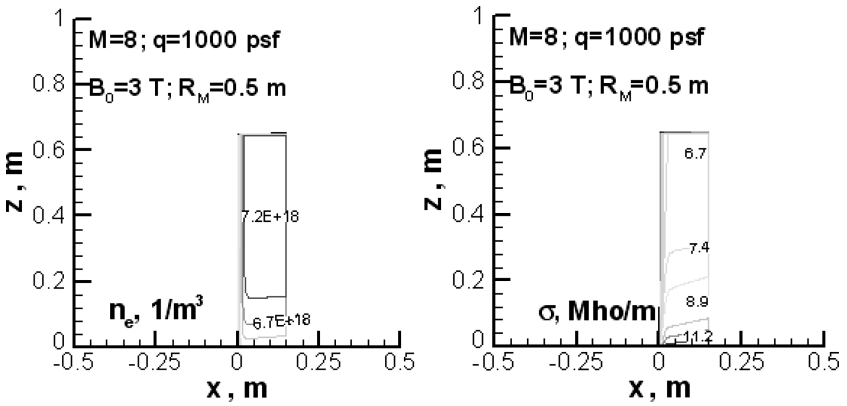

Fig. 3 Profiles at Mach 8, $q = 1000$ psf (47.88 kPa), $L_b = 0.65$ m, and $Q_b = 10$ MW/m^3, with the tilt angle $\alpha = \pi/2$. Electron number density (left) and Electrical conductivity (right).

normal force on the surface

$$F_z = \int_0^{X_{\max}} (p(x,0) - p_0)\,\mathrm{d}x \tag{10}$$

converges (which requires $X_{\max}$ to be sufficiently large) and that there is negligible outflow through the upper boundary, so that the drag/thrust force can be computed as

$$F_x = \int_0^{Z_{\max}} \left[(\rho u^2 + p)_{x_{\max}} - \rho_0 u_0{}^2 - p_0\right]\mathrm{d}z \tag{11}$$

Specifically, $X_{\max} = 8$ m, and the number of grid points in the x direction was $N_x = 4000$ in all cases; depending on the Mach number, $Z_{\max}$ was between 2 and 3 m, and the number of grid points in the z direction, N_z, varied from 300 to 450. When the number of grid points in each direction was changed by a factor of two, the results were found to change by less than 1%.

Because the flow is in the positive x direction, $F_x > 0$ corresponds to thrust and $F_x < 0$ to drag, where $\Delta D = |F_x|$. In all computed cases, flow turning and heating resulted in increased surface pressure, so that $F_z > 0$. If the MHD region is positioned on the upper surface of the vehicle (Fig. 1), this would create a downward force, whereas placing MHD devices on the bottom surfaces (Fig. 1) would increase lift. In the paragraphs to follow, we will assume the latter case (where Fig. 2 is flipped over) and the force $F_z > 0$ will be called the lift force, $F_z = \Delta L$.

III. Results of Computations

Figure 3 shows the electron density and conductivity profiles at Mach 8, with electron beam penetration depth $L_b = 0.65$ m and the beam power deposition density $Q_b = 10$ MW/m^3, with the tilt angle $\alpha = \pi/2$. As seen in Fig. 3, the electron density is up to 7×10^{18} m$^{-3} = 7 \times 10^{12}$ cm^{-3}, and the electrical conductivity is about 5–10 mho/m. At these relatively high electron number densities and low gas densities (typically 4×10^{-3} of the standard atmospheric density), the electron attachment is negligible compared with the electron–ion dissociative recombination. Therefore, the number density of negative ions is much lower than that of electrons. In the recombination-controlled regime, the steady-state electron density is proportional to the square root of ionization rate (which, in turn, is proportional to Q_b) and does not explicitly depend on gas density. Consequently, the electrical conductivity is proportional to the square root of Q_b and inversely proportional to the gas density.

The drag force F_x and the heating rate per unit length in the spanwise direction, P_b, due to electron beams only, in the absence of MHD, are shown in Fig. 4 as functions of Q_b. Figure 5 shows the thrust force F_x, the heating rate due to electron beams, P_b, and the power deposited per unit length in the spanwise direction due to MHD, as functions of Q_b for an accelerator with tilt angle $\alpha = \pi/2$ and $\chi = E_y/u_0 B_0 = 1$. The MHD power deposition was

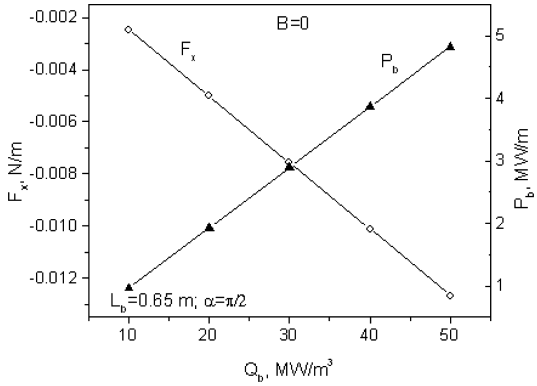

Fig. 4 Drag force F_x and heating rate per unit length in spanwise direction, P_b, due to electron beams only, in the absence of MHD, as functions of Q_b.

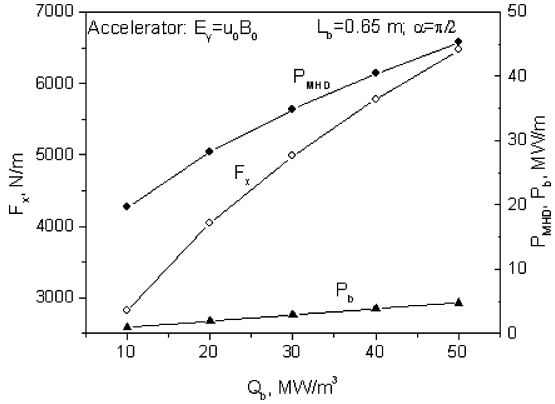

Fig. 5 Thrust force F_x, heating rate due to electron beams, P_b, and power deposited per unit length in spanwise direction due to MHD, as functions of Q_b for accelerator with tilt angle $\alpha = \pi/2$ and $\chi = E_y/u_0 B_0 = 1$.

calculated as

$$P_{\mathrm{MHD}} = \int_{\text{electrode}} j_y E_y\,\mathrm{d}x\,\mathrm{d}z$$

and the total power deposited per unit length in the spanwise direction due to both electron beams and MHD is equal to $P_{\mathrm{MHD}} + P_b$. As an example of the energy balance, at $Q_b = 10$ MW/m^3, $E_y = u_0 B_0 = 7253.8$ V/m, and $P_b = 0.965$ MW/m, the MHD-deposited power is $P_{\mathrm{MHD}} = 19.64$ MW/m, the rate of work done by $\boldsymbol{j} \times \boldsymbol{B}$ forces is $P_{j \times B} = 6.96$ MW/m, the joule heating rate is $P_J = 4.53$ MW/m, and the power spent on vibrational excitation of molecules is $P_{\mathrm{vib}} = 8.15$ MW/m, so that $P_{\mathrm{MHD}} = P_{j \times B} + P_J + P_{\mathrm{vib}}$.

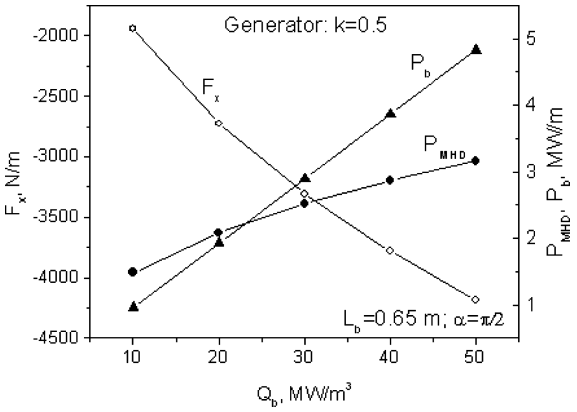

Fig. 6 Drag force F_x, heating rate due to electron beams, P_b, and MHD extracted power per unit length in spanwise direction, as functions of Q_b for generator with tilt angle $\alpha = \pi/2$ and $k = 0.5$.

Figure 6 shows the drag force F_x, the heating rate due to electron beams, P_b, and the MHD extracted power per unit length in the spanwise direction, as functions of Q_b for a generator with tilt angle $\alpha = \pi/2$ and $k = 0.5$. Note that when $P_{\text{MHD}} > P_b (Q_b < 23\ \text{MW/m}^3)$, net power is extracted from the flow. As an example of the energy balance, at $Q_b = 10\ \text{MW/m}^3$ and $P_b = 0.965$ MW/m, the rate of work done by $\boldsymbol{j} \times \boldsymbol{B}$ forces is $P_{j \times B}$ MW/m, the MHD-extracted power is $P_{\text{MHD}} = 1.486$ MW/m, the Joule heating rate is $P_j = 1.67$ MW/m, and the power spent on vibrational excitation of molecules is $P_{\text{vib}} = 1.38$ MW/m, so that $P_{j \times B} = P_{\text{MHD}} = P_J + P_{\text{vib}}$.

Note that a considerable fraction of power is spent on vibrational excitation of air molecules. Vibrational relaxation in the model (Refs. 1–3 and 5) is due to collisions of excited nitrogen molecules with molecular and atomic oxygen. The estimated mole fraction of atomic oxygen produced by electron beam-induced dissociation of atomic oxygen and by the dissociative attachment of low-energy plasma electrons is on the order of 10^{-3}. Under the low-temperature ($T = 500-700$ K), low-density [$(4-6) \times 10^{-3}$ of the standard atmospheric density] conditions considered in this work, the flow residence time in the 6–8 m long region relevant to the computations of aerodynamic forces turned out to be too short for any significant vibrational relaxation. Thus, the energy deposited into the vibrational mode in the plasma region becomes frozen and excluded from gasdynamic effects.

As discussed in Subsec. II.A., in the case of nonuniform velocity and magnetic field, Ohm's law (8) applies with local values of conductivity, velocity, magnetic field, and Hall parameters. However, the applied electric field strength E_y is constant throughout the MHD region. Therefore, depending on the value of E_y, or the parameter $\chi = E_y/u_0 B_0$, some regions of the flow would have a positive current and would experience acceleration, whereas in other regions, where $u_x B_z < E_y$, the current would be reversed, resulting in decelerating $j_y B_z$ force. To illustrate the flexibility of MHD control by changing the parameter $\chi = E_y/u_0 B_0$, a series of computations was run for Mach 8, $\alpha = \pi/2$, and $Q_b = 10\ \text{MW/m}^3$. Figure 7 shows how the profile of $\boldsymbol{j} \times \boldsymbol{B}$ forces change with $\chi = E_y/u_0 B_0$, from predominantly decelerating forces at low χ to a combination of deceleration near the surface and acceleration of the outer flow at $\chi \approx 0.5$, to only acceleration at $\chi = 1$. Figure 8 shows the flowfield (temperature and velocity contour lines) in the case $\chi = 1$; the oblique shock can be seen to originate at the edge of the heated MHD region. The computed force F_x vs the parameter χ is shown in Fig. 9, together with the MHD-deposited power P_{MHD}. As can be seen in Fig. 9, at low χ the force F_x is negative (drag), whereas at high χ thrust is created, $F_x > 0$.

As stated in Sec. II, the modeling in this work was for an inviscid flow. Because the plasma and MHD region extends 0.65 m from the surface, that is, well beyond a typical boundary layer, the inviscid analysis is reasonable. Note, however, that the decelerating $\boldsymbol{j} \times \boldsymbol{B}$ forces in the cases of MHD generator or low-χ accelerator, in conjunction with joule heating, can potentially cause accelerated

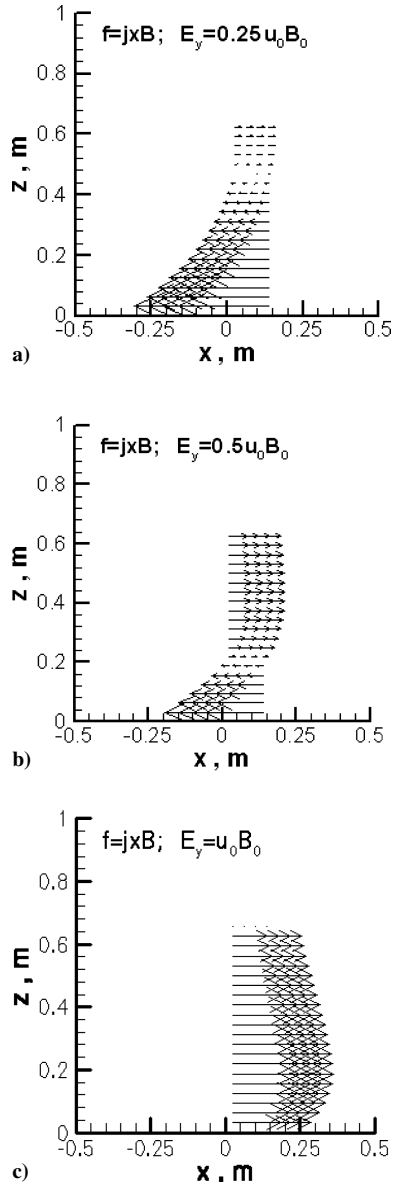

Fig. 7 Profiles of $j \times B$ forces at Mach 8, $\alpha = \pi/2$, and $Q_b = 10\ \text{MW/m}^3$ at a) $\chi = E_y/u_0 B_0 = 0.25$, b) $\chi = 0.5$, and c) and $\chi = 1$.

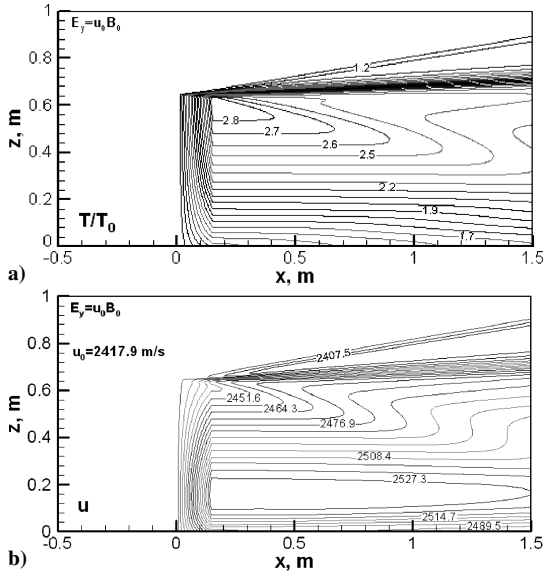

Fig. 8 Accelerator with $\chi = 1$, at Mach 8, $\alpha = \pi/2$, and $Q_b = 10\ \text{MW/m}^3$. Static temperature (upper plot) and Velocity (lower plot).

boundary-layer growth and flow separation, whereas the accelerating $\boldsymbol{j} \times \boldsymbol{B}$ forces in the cases of high-χ accelerator could suppress separation. These important effects should be studied in the future with viscous fluid dynamic models.

Varying the tilt angle α of the magnetic field increases the flexibility of MHD control. Figures 10 and 11 show the corresponding $\boldsymbol{j} \times \boldsymbol{B}$ forces in representative generator ($k = 0.5$ and $Q_b = 10$ MW/m^3) and accelerator ($\chi = 1$ and $Q_b = 10$ MW/m^3) cases for the magnetic field with left ($\alpha = \pi/4$) and right ($\alpha = 3\pi/4$) tilt.

To quantify the effects of varying tilt angle as well as of the electron beam power on lift and drag forces, pressure on the surface was computed, as shown in Figs. 12–15. As seen in Figs. 12–15, the relaxation of pressure occurs over long distances downstream of the MHD region, due to the high Mach number of the flow. Indeed, the relaxation distance should be proportional to the Mach

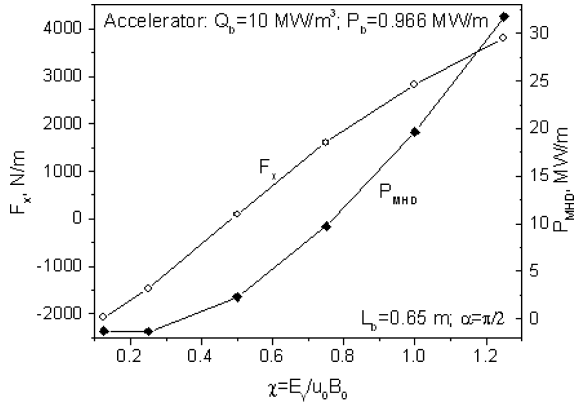

Fig. 9 Computed drag/thrust force F_x and the MHD-deposited power P_{MHD} vs parameter χ in accelerator case at Mach 8, $\alpha = \pi/2$, and $Q_b = 10$ MW/m^3.

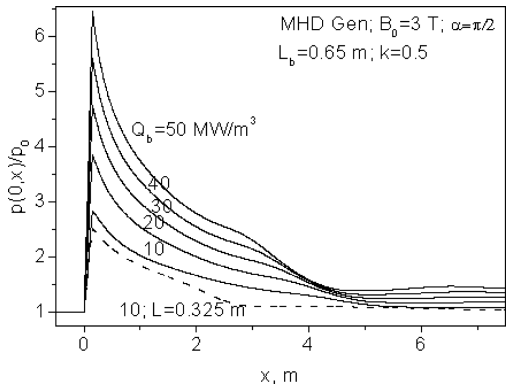

Fig. 12 Surface pressure profiles for MHD generator with $k = 0.5$ and tilt angle $\alpha = \pi/2$ at different electron beam power densities Q_b.

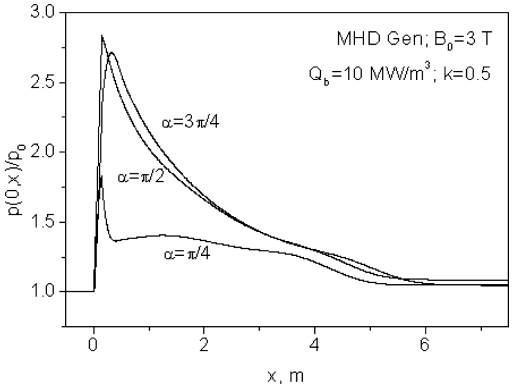

Fig. 13 Surface pressure profiles for MHD generator with $k = 0.5$ and electron beam power density $Q_b = 10$ MW/m^3 at different tilt angles.

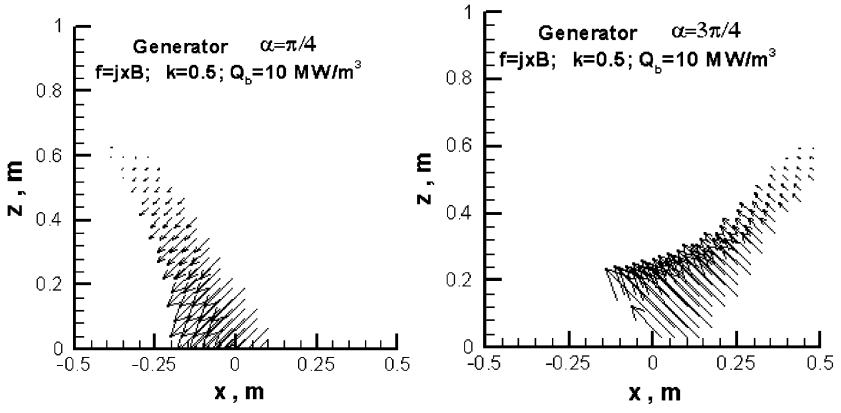

Fig. 10 Representative generator case $j \times B$ forces at $k = 0.5$ and $Q_b = 10$ MW/m^3, with left ($\alpha = \pi/4$) and right ($\alpha = 3\pi/4$) magnetic field tilt angle.

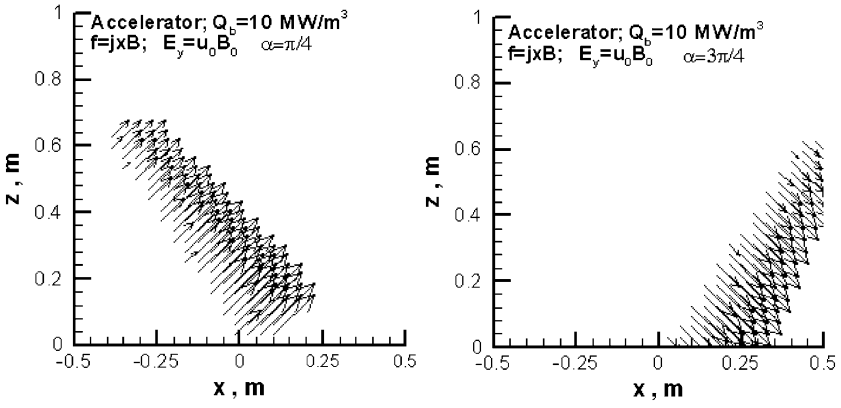

Fig. 11 Representative accelerator case $j \times B$ forces at $\chi = 1$ and $Q_b = 10$ MW/m^3, with left ($\alpha = \pi/4$) and right ($\alpha = 3\pi/4$) magnetic field tilt angle.

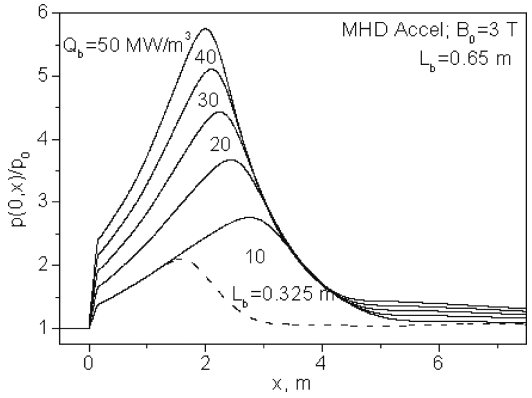

Fig. 14 Surface pressure profiles for MHD accelerator with $\chi = 1$ and tilt angle $\alpha = \pi/2$ at different electron beam power densities Q_b.

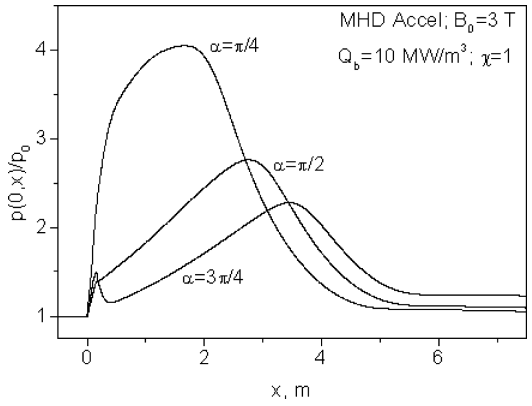

Fig. 15 Surface pressure profiles for MHD accelerator with $\chi = 1$ and electron beam power density $Q_b = 10$ MW/m^3 at different tilt angles.

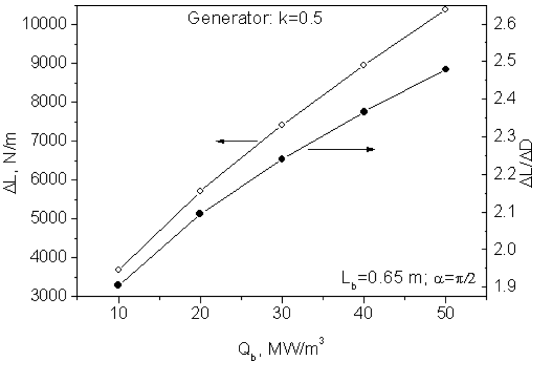

Fig. 16 Normal force ΔL and lift/drag ratio $\Delta L/\Delta D$ for MHD generator at $k = 0.5$ and tilt angle $\alpha = \pi/2$ vs electron beam power density Q_b.

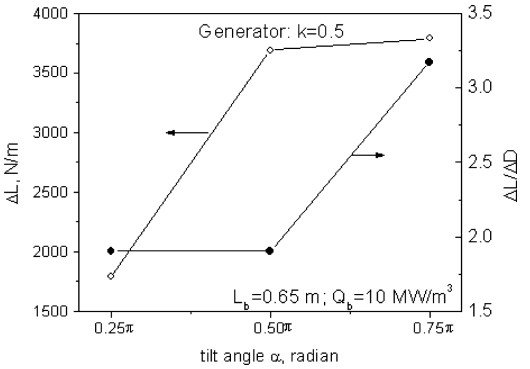

Fig. 17 Normal force ΔL and lift/drag ratio $\Delta L/\Delta D$ for MHD generator at $k = 0.5$ and electron beam power density $Q_b = 10$ MW/m^3 vs tilt angle α.

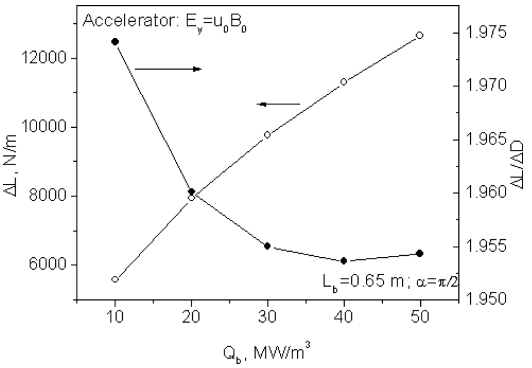

Fig. 18 Normal force ΔL and lift/thrust ratio $\Delta L/\Delta D$ for MHD accelerator at $\chi = 1$ and tilt angle $\alpha = \pi/2$ vs electron beam power density Q_b.

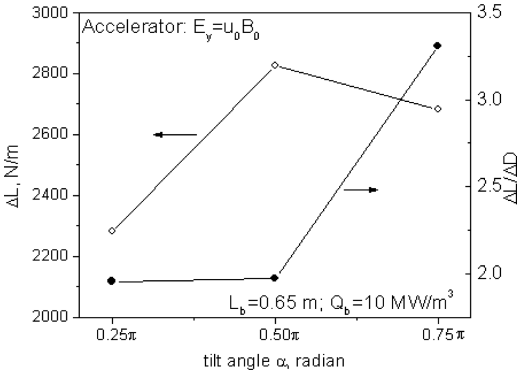

Fig. 19 Normal force ΔL and lift/thrust ratio $\Delta L/\Delta D$ for MHD accelerator at $\chi = 1$ and electron beam power density $Q_b = 10$ MW/m^3 vs tilt angle α.

number: the ratio of flow velocity to the speed with which transverse pressure disturbances equilibrate, that is, the speed of sound, as well as to the transverse dimension of the perturbation, that is, the beam penetration depth L_b. The latter is confirmed by the fact that reducing the beam penetration depth by one-half cuts the pressure relaxation distance also approximately by one-half, as seen in the lower curves in Figs. 12 and 14.

The corresponding values of lift and drag/thrust forces and their ratio $\Delta L/\Delta D$ were computed as discussed in Subsec. II.B. As seen in Figs. 16–19, the normal force created by the MHD region is substantially stronger than the drag/thrust force, with the ratio $\Delta L/\Delta D$ increasing from about 2 with magnetic field tilted against the flow or normal to the surface to more than 3 with aft-tilted magnetic field. The strong normal force is due to the increase in static pressure, which, in the generator cases, is caused primarily by the joule heating and energy deposition by the electron beam, as well as by the retarding Lorentz force. The additional drag force, on the other hand, is caused primarily by the retarding Lorentz force. Therefore, the normal force turns out to be substantially stronger than the increase in drag (Figs. 16 and 17). In the recombination-controlled regime, the electron density and the electrical conductivity are proportional to the square root of the ionization rate, whereas the beam-induced heating is proportional to the electron beam power deposition Q_b. Because at a constant load factor, the ratio of joule heating to the rate of work by Lorentz force is kept constant, therefore, increasing Q_b favors overall heating effects vs Lorentz force effects, and the ratio $\Delta L/\Delta D$ increases with Q_b, as seen in Fig. 16.

In the accelerator cases, the accelerating Lorentz force tends to mitigate the pressure rise caused by heating. Additionally, operation at $\chi = E_y/(u_0 B_0) = 1$ makes the current density $j_y = \tilde{\sigma}(E_y - u_x B_z)$ small and thereby reduces the ratio of joule heating rate $(j_y^2/\tilde{\sigma})$ to the rate of work by Lorentz force $(j_y B_z u_x)$. These two factors explain why the ratio $\Delta L/\Delta D$ in the accelerator cases (Fig. 18) is lower than it is in the generator cases (Fig. 16).

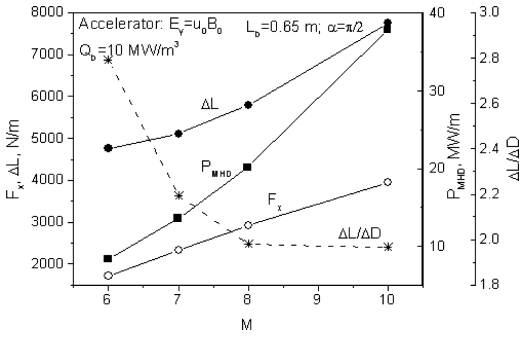

Fig. 20 Drag F_x and lift ΔL forces, their ratio ($\Delta L/\Delta D$), and MHD extracted power vs Mach number for MHD generator with $k = 0.5$, tilt angle $\alpha = \pi/2$, and electron beam power density $Q_b = 10$ MW/m^3.

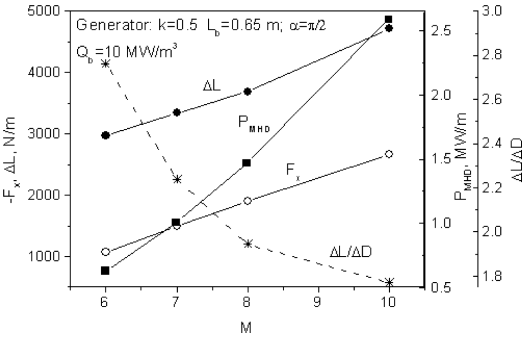

Fig. 21 Thrust F_x and lift ΔL forces, their ratio ($\Delta L/\Delta D$), and MHD deposited power vs Mach number for MHD accelerator with $\chi = 1$, tilt angle $\alpha = \pi/2$, and electron beam power density $Q_b = 10$ MW/m^3.

The results of computations performed for representative generator and accelerator cases in the range of Mach numbers from Mach 6 to Mach 10 are summarized in Figs. 20 and 21. As seen in Figs. 20 and 21, whereas both tangential (drag for generators and thrust for accelerators) and normal (lift) forces tend to increase with Mach number, the ratio $\Delta L/\Delta D$ monotonically decreases with Mach number. These trends can be qualitatively explained as follows. At a constant freestream dynamic pressure, higher velocity implies lower gas density. Because in the recombination-controlled regime the electron density is fully determined by the electron beam power deposition density, the electron density is constant at constant Q_b and the electrical conductivity, proportional to the ratio of electron and molecule number densities, increases with Mach number. Consequently, at constant k (for generators) or χ (for accelerators), both the electric current density [$j_y \approx (1-k)\tilde{\sigma} u_x B_z$ for generators and $j_y \approx (\chi - 1)\tilde{\sigma} u_x B_z$ for accelerators] and the Lorentz force [$j_y B_z \approx (1-k)\tilde{\sigma} u_x B_z^2$ for generators and $j_y B_z \approx (\chi - 1)\tilde{\sigma} u_x B_z^2$ for accelerators] increase with Mach number, resulting in the tangential force increase seen in Figs. 20 and 21. As noted earlier, the ratio $\Delta L/\Delta D$ depends on the relative magnitude of heating vs Lorentz force work rate. In the cases shown in Figs. 20 and 21, the ratio of joule heating rate and the rate of work by Lorentz force was kept constant by the constant k or χ. However, at constant electron beam power deposition density Q_b, the magnitude of the beam-induced heating diminishes relative to the growing rate of work by Lorentz force as the Mach number increases. Therefore, the overall heating effects decrease relative to the Lorentz force effects, resulting in the decease in $\Delta L/\Delta D$ with Mach number seen in Figs. 20 and 21.

IV. Conclusions

In this paper, we have proposed a concept of aerodynamic control of external hypersonic flow with MHD devices where ionization is created by electron beams. Arrays of MHD devices can be positioned, for example, at the bottom of the vehicle aft of the combustor, where the density is close to that in the freestream, and/or on the top of the vehicle. The preliminary modeling based on inviscid flow approximation and simplified assumptions regarding magnetic field and electron beams has demonstrated that the accelerating or decelerating Lorentz forces together with the joule heating of the flow can indeed generate substantial tangential and normal forces. The tangential forces and their profiles are controlled by the ratio χ of the applied electric field to the product of freestream velocity and the magnetic field at the surface and by the tilt angle α of the magnetic field.

The normal (lift) force created by the MHD region turned out to be substantially stronger than the drag/thrust force. The lift/drag (for MHD generators) or lift/thrust (for accelerators) ratios range from about 2 to more than 3 and decrease with Mach number. These findings can be explained by the static pressure increase caused by the joule heating and the electron beam energy deposition. The magnitude of the heating-caused rise in normal pressure force is greater that the tangential Lorentz force, but as the Lorentz force grows with the Mach number, the relative magnitude of heating-caused normal force diminishes with respect to the tangential force.

The preliminary modeling in this work used an inviscid flow model. However, the decelerating Lorentz forces in the cases of MHD generator or low-χ accelerator, in conjunction with gas heating, can potentially cause boundary-layer growth and flow separation, whereas the accelerating Lorentz forces in the cases of the high-χ accelerator could suppress separation. These important effects should be studied in the future with viscous fluid dynamic models.

Acknowledgments

This work was supported by the Air Force Office of Scientific Research (John Schmisseur). The authors express their gratitude to Richard B. Miles and David M. Van Wie for valuable discussions and advice.

References

[1]Macheret, S. O., Shneider, M. N., Miles, R. B., and Lipinski, R. J., "Electron Beam Generated Plasmas in Hypersonic Magnetohydrodynamic Channels," *AIAA Journal*, 2001, Vol. 39, No. 6, pp. 1127–1136.

[2]Macheret, S. O., Shneider, M. N., and Miles, R. B., "Magnetohydrodynamic Control of Hypersonic Flow and Scramjet Inlets Using Electron Beam Ionization," *AIAA Journal*, Vol. 40, No. 1, 2002, pp. 74–81.

[3]Macheret, S. O., Shneider, M. N., and Miles, R. B., "MHD Power Extraction from Cold Hypersonic Air Flow with External Ionizers," *Journal of Propulsion and Power*, Vol. 18, No. 2, 2002, pp. 424–431.

[4]Macheret, S. O., Shneider, M. N., and Miles, R. B., "Magnetohydrodynamic and Electrohydrodynamic Control of Hypersonic Flows of Weakly Ionized Plasmas," *AIAA Journal*, Vol. 42, No. 7, 2004, pp. 1378–1387.

[5]Shneider, M. N., Macheret, S. O., and Miles, R. B., "Analysis of Magnetohydrodynamic Control of Scramjet Inlets," *AIAA Journal*, Vol. 42, No. 11, 2004, pp. 2303–2310.

[6]Macheret, S. O., Shneider, M. N., and Miles, R. B., "Optimum Performance of Electron Beam Driven MHD Generators for Scramjet Inlet Control," AIAA Paper 2003-3763, June 2003.

[7]Murray, R. C., Vasilyak, L., Carraro, M. R., Zaidi, S. H., Macheret, S. O., Shneider, M. N., and Miles, R. B., "Observation of MHD Effects With Nonequilibrium Ionization in Cold Supersonic Air Flows," AIAA Paper 2004-1025, Jan. 2004.

[8]Kuranov, A. L., and Sheikin, E. G., "MHD Control on Hypersonic Aircraft under AJAX Concept: Possibilities of MHD Generator," AIAA Paper 2002-0490, Jan. 2002.

[9]Vatazhin, A., Kopchenov, V., and Gouskov, O., "Some Estimations of Possibility to Use the MHD Control for Hypersonic Flow Deceleration," AIAA Paper 99-4972, Nov. 1999.

[10]Kopchenov, V., Vatazhin, A., and Gouskov, O., "Estimation of Possibility of Use of MHD Control in Scramjet," AIAA Paper 99-4971, Nov. 1999.

[11]Vatazhin, A., Kopchenov, V., and Gouskov, O., "Numerical Investigation of Hypersonic Inlets Control by Magnetic Field," *The 2nd Workshop on Magneto- and Plasma Aerodynamics in Aerospace Applications*, Institute of High Temperatures, Russian Academy of Sciences, Moscow, 2000, pp. 56–63.

[12]Brichkin, D. I., Kuranov, A. L., and Sheikin, E. G., "The Potentialities of MHD Control for Improving Scramjet Performance," AIAA Paper 99-4969, Nov. 1999.

[13]Bityurin, V. A., Klimov, A. I., Leonov, S. B., Bocharov, A. N., and Lineberry, J. T., "Assessment of a Concept of Advanced Flow/Flight Control for Hypersonic Flights in Atmosphere," AIAA Paper 99-4820, Nov. 1999.

[14]Rosa, R. J., *Magnetohydrodynamic Energy Conversion*, McGraw-Hill, New York, 1968, Chaps. 3, 4.